Near- and sub-barrier fusion of ^{58}Ni with ^{58}Ni

M. Beckerman, J. Ball, H. Enge, M. Salomaa, A. Sperduto, S. Gazes, A. DiRienzo, and J. D. Molitoris
Laboratory for Nuclear Science, Massachusetts Institute of Technology, Cambridge, Massachusetts 02139
(Received 7 July 1980)

Differential cross sections for evaporation residue formation following the complete fusion of ^{58}Ni with 187.6 to 220 MeV ^{58}Ni ions were measured with high precision using a velocity selector together with a counter telescope. The resulting cross sections for complete fusion ranged in magnitude from 50 μb at 93.3 MeV to 230 mb at 108.9 MeV (c.m.). The cross sections for complete fusion at sub-barrier energies were shown to be far greater than those predicted by standard barrier penetration models.

[NUCLEAR REACTIONS Complete fusion, ^{58}Ni + ^{58}Ni, E = 187.6 to 220 MeV lab, measured $\sigma(E,\theta)$ for evaporation residues.]

I. INTRODUCTION

In this paper we present results of measurements of cross sections for evaporation residue formation following complete fusion of ^{58}Ni with 187.6 to 220 MeV ^{58}Ni ions. These measurements are the first in a series of measurements of complete fusion excitation functions for massive systems at near- and sub-barrier energies, and of complementary reaction processes. The aim of these measurements is to obtain high quality data which will provide insight into the interplay between fusion dynamics and the underlying nuclear structure.

Evaporation residue differential cross sections were measured using the MIT-BNL Velocity Selector in conjunction with a gas telescope. Evaporation residues have been measured previously using gas telescopes,[1-4] time-of-flight (TOF) spectrometers,[5-7] magnetic spectrographs,[8] and x-ray techniques.[9,10] By using a velocity selector the measurement of differential cross sections for the forward-peaked evaporation residues to zero degrees becomes possible. This capability, in turn, enables the determination of complete fusion excitation functions at near- and sub-barrier energies with higher precision than can be done with systems for which the intense elastic scattering prevents operation at sufficiently small angles. Since these are the first measurements of fusion excitation functions using the present technique, this paper focuses upon the experimental method, the accuracy which is achieved, and improvements which can be made. The ^{58}Ni + ^{58}Ni process is representative of a massive, symmetric closed shell reaction. Complete fusion excitation functions for ^{58}Ni + ^{64}Ni and ^{64}Ni + ^{64}Ni have also been measured. A summary of the most salient features of these data and their significance has been presented elsewhere.[11]

The detection system consisting of scattering chamber monitors, a velocity selector system, and a gas $\Delta E - E$ telescope is described in Sec. II A. The fusion measurements were preceded by elastic scattering measurements performed to calibrate the detection system. The procedures for calibration and fusion measurements are described in Sec. II B. The absolute efficiencies and associated experimental uncertainties are discussed in Sec. III A. At the energies involved in these measurements, fission competition is negligible and the complete fusion cross sections equal the evaporation residue cross sections. The results of the evaporation residue cross section measurements are presented and discussed in Sec. III B, and the work is summarized in Sec. IV.

II. EXPERIMENTAL METHOD

A. Apparatus

Scattering Chamber. Two silicon surface barrier detectors mounted in the scattering chamber at angles of 21.8° (see Fig. 1) with respect to the beam axis provided beam normalization and monitoring. These detectors subtended solid angles of 0.045 msr at the target and had angular acceptances of 0.4° taking into account multiple scattering in the target and the finite size of the beam spot. The beam was limited to an area of 1.5 × 2.5 mm by two pairs of cylindrical carbon slits placed in front of the target. We maintained beam spot quality by minimizing the current to these slits while simultaneously maximizing the transmitted current. The solid angle and angular acceptance of the $\Delta E - E$ telescope were determined by the ion optics of the velocity selector system. The telescope angle was defined to better than 0.1° at small scattering angles and 0.2° at large ($\gtrsim$15°) scattering angles.

Velocity selector system. The velocity selector system,[12] shown in Fig. 1, consisted of a quadrupole doublet, electrostatic deflector, magnetic

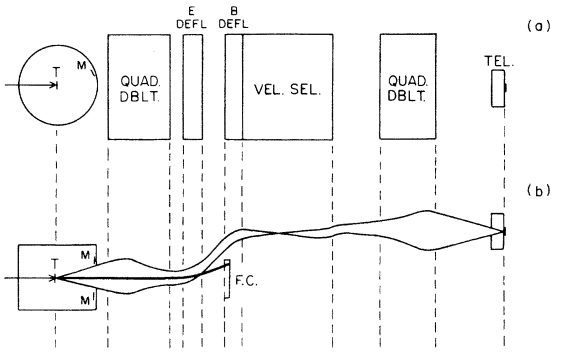

FIG. 1. (a) Schematic (top) view of the detection system, and (b) corresponding side view of representative trajectories. The total length of the system, from target to telescope E detector, is 4.4 m; the total vertical shift of the trajectories is 5 cm. Thick solid curve represents full-energy beamlike ions terminated in a Faraday cup; two thinner curves denote paths of ions of mass, velocity, and charge state for which the velocity selector fields were set. Note that the magnetic deflector, which brings transmitted ions back to the horizontal, is simply the leading portion of the magnetic field of the velocity selector proper.

deflector, velocity selector, and a second quadrupole doublet. The first quadrupole doublet was used to increase the solid angle and image the beam spot at the center of the velocity selector. The electrostatic deflector was used to displace upward the reaction products of interest, bringing them to the center line of the velocity selector, thereby separating them from the intense flux of the full-energy beamlike ions. (The beamlike ions were collected in a Faraday cup; the ions of interest were bent back to the horizontal by the magnetic deflector.) The velocity selector had crossed electric and magnetic fields and was used to remove all ions except those having the desired velocity. The second quadrupole doublet was used to reimage the ions onto the telescope E detector. (The telescope axis was shifted slightly upward from the velocity selector centerline to compensate for differences in spatial extension of the electric and magnetic fields.) Some beamlike particles scattered from elements of the front part of the velocity selector system, and from slits into the velocity selector proper, with a velocity which enabled their transmission; these ions were well separated from the products of interest in the $\Delta E - E$ spectrum.

$\Delta E - E$ telescope. A telescope consisting of a gas ΔE counter and a solid-state E counter was used to identify the evaporation residues. The ΔE section consisted of a proportional chamber containing isobutane at 20 mm Hg and the E counter was a 450 mm^2 silicon surface-barrier detector mounted at the rear of the gas counter. A 70 μ thick polypropelene window supported on a 90% transmission mesh served as the entrance aperture.

Electronics. The two monitor E signals and the telescope ΔE and $(E - \Delta E)$ signals were processed by conventional electronics, and collected and stored on-line in the BNL Sigma-7 Computer System. A 128×64 array was used for the telescope spectra. A pileup rejection circuit was added for use at far sub-barrier energies where the beam-tail events could give rise to a substantial pileup background.

B. Procedure

We recall that the magnetic rigidity $B\rho$ of ions of mass A and charge state q moving in a direction perpendicular to the magnetic field B with kinetic energy E_K is proportional to $(E_K A)^{1/2}/q$ (see, for example, Ref. 13). The (crossed) electric field which enables ions of velocity v to pass through the filter undeflected is $E = B_0 v$, where B_0 is the magnetic field in the velocity selector. Due to their common dependence upon p/q, where p is the ion momentum, the quadrupole fields also are proportional to the field B_0. As a result, the field setting equations of the velocity selector system take the simple form $B_0 = C_0 (E_K A)^{1/2}/q$, voltage on the deflector plates $V = C_V B_0 v$, and quadrupole fields $B_i = C_i B_0$.

In the geometry shown in Fig. 1 the radius of curvature in the uncompensated magnetic and electric fields is $\rho = 190$ cm. For q we employed the universal expression[14,15] for the mean charge state $\bar{q}$ of heavy ions passing through solid targets

$$\bar{q}(v_r) = Z(1 + v_r^{-1/k})^{-k}, \tag{1}$$

where the reduced velocity $v_r = v/v_0 Z^{\alpha}$. The atomic number of the ion is Z, $v_0 = 3.6 \times 10^8$ cm/sec, $\alpha = 0.45$, and $k = 0.6$. The charge-state specification will be discussed further in Sec. III. In the present experiment $\bar{q}$ varied from 22 to 28, B_0 ranged from 2.8 to 3.4 kG, and V from 80 to 105 kV.

With the above-mentioned setup, differential cross sections were measured for elastic scattering of ^{127}I on ^{197}Au and for evaporation residue formation following complete fusion of ^{58}Ni and ^{58}Ni (see Table I).

Elastic scattering. ^{127}I + Au elastic scattering yields were used in order to calibrate the detection system with ions of similar kinetic energy, mass and atomic numbers, and mean charge states as the evaporation residues. Starting with values for the field constants C_0, C_V, and C_i de-

TABLE I. Summary of types of measurements performed.

Measurement	Projectile and bombarding energy range	Targets and their composition
Elastic scattering	^{127}I 80 to 120 MeV	Au 90 to 170 μg/cm^2
Evaporation residues	^{58}Ni 187 to 220 MeV	^{58}Ni (99.927%) 125 to 225 μg/cm^2 [a]

[a] Self-supported or on 10 μg/cm^2 carbon backings.

termined from RAYTRACE[16] calculations, the fields were fine-tuned to maximize $y_{el} = N_{el}^{tel}/N_{el}^{mon}$, the elastic scattering yield in the counter telescope relative to that in the target chamber monitors. This procedure was repeated at a number of recoil energies and the resulting empirically refined field constants were used for all subsequent measurements. The absolute efficiencies f of the detection system were obtained from the peak yields

$$f = y_{el} \frac{\frac{d\sigma^{Ruth}}{d\Omega}(\theta_{mon})}{\frac{d\sigma^{Ruth}}{d\Omega}(\theta_{tel})}, \quad (2)$$

where $(d\sigma^{Ruth}/d\Omega)(\theta_a)$ denotes the calculated Rutherford cross section at angle θ_a. Velocity (energy) acceptance profiles of the system were measured at representative energies. This was done by keeping the filter set for a given velocity and varying the beam velocity in small steps from well below to well above that given velocity. Widths σ_v were then extracted. Checks performed using the Au targets of various thicknesses (see Table I) confirmed that spreading due to multiple scattering in the targets was small. The calibration measurements thus provided a set of values $\{f, \sigma_v\}(v_r)$, which was used to convert the evaporation residue yields to absolute cross sections.

Evaporation residues. The evaporation residue recoil kinetic energy spectra were measured at representative recoil angles and bombarding energies. These spectra were determined by sweeping the velocities transmitted by the filter over the ranges spanned by the evaporation residues. The evaporation residue angular distributions were measured from 0° to 6° in 1° steps at representative bombarding energies. We supplemented these data with additional zero degree differential cross section data taken at intermediate energies. The evaporation residue differential cross sections were extracted from the evaporation residue yields $y_{ER} = N_{ER}^{tel}/N_{el}^{mon}$ using

$$\frac{d\sigma^{ER}}{d\Omega}(\theta_{ER}) = y_{ER} f^{-1} \frac{d\sigma^{Ruth}}{d\Omega}(\theta_{mon}). \quad (3)$$

III. EXPERIMENTAL RESULTS

A. Calibration

The values for $f^{-1}(v_r)$ deduced from the elastic scattering measurements are displayed in Fig. 2. The smooth curve drawn through the data represents the absolute efficiencies regarded as a function of reduced velocity; the corresponding kinetic energies were given for the abscissa for ease in visualization. The root-mean-square (rms) deviation of the data from the smooth curve is 3.6%, and this was taken as the error associated with the calibration measurements. This uncertainty is larger than the statistical errors, and is attributed to variations in beam tuning. There is a gradual increase in the efficiencies as the ion recoil energy increases. This is due to charge-state effects, and will be discussed further.

A representative velocity (energy) acceptance profile is presented in Fig. 3. The central value of the distribution gives the efficiency presented in Fig. 2 for that energy. The full width at half maximum (FWHM) of the distribution is 8.6 MeV, or 8.9% of the central recoil kinetic energy. Similar, proportional results were found for other energy acceptance profiles. Since small variations in shape were observed to occur among these distributions, the actual integrations of the recoil kinetic energy spectra of the evaporation residues were done using widths of equivalent, normalized distributions of fixed shape.

Equilibrium charge-state measurements (e.g., Refs. 17 and 18) have revealed that broad distributions of charge state occur with no single charge state accounting for more than about 20% of the total yield. RAYTRACE calculations[19] have shown

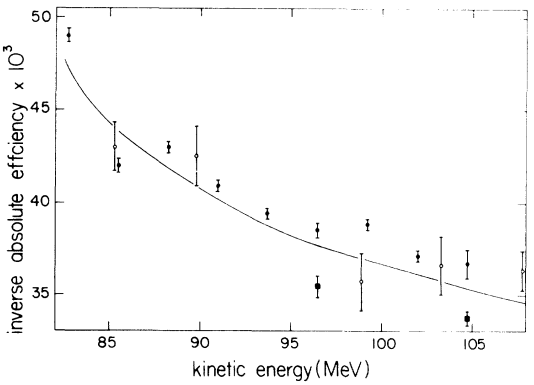

FIG. 2. Plot of f^{-1} as a function of the ^{127}I recoil kinetic energy. Note the greatly expanded ordinate. Different symbol types represent results obtained from distinct series of calibration measurements. Error bars in Figs. 1–5 denote statistical errors.

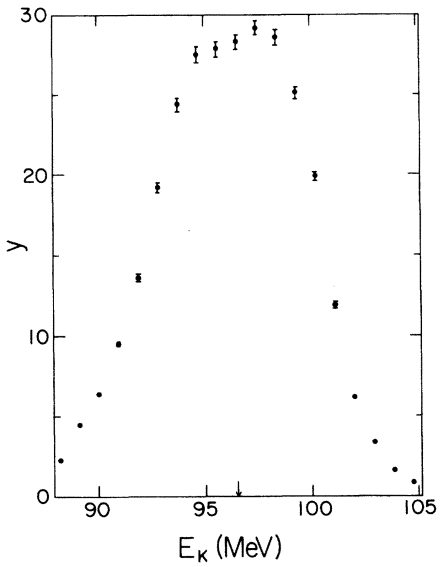

FIG. 3. Plot of ^{127}I + Au elastic scattering yield versus ^{127}I recoil kinetic energy. The arrow shows the central energy for which the fields were set.

that many charge states are transmitted through the detection system; maximum efficiencies occur for $q=\bar{q}$, and $\bar{q}+1$ charge states when the system is set for $q=\bar{q}$, and the efficiencies decrease fairly uniformly as the charge states either decrease or increase away from $\bar{q}$. These two aspects folded together give rise to the observed efficiencies and corresponding effective solid angles. The effective solid angle, i.e., the solid angle that would apply if all ions had the same A, v, and q, ranged from 1.1 msr at 80 MeV to 1.3 msr at 110 MeV.

The principal source of uncertainty in determining the absolute cross sections is departures of the actual mean charge states from those calculated using Eq. (1). Systematic departure may be expected due to the inadequate energy dependence and neglect of any dependence upon target material. The former are taken into account automatically in the calibration procedure, and together with the chromatic aberrations (also taken into account) contribute to the energy dependence of the efficiencies as seen in Fig. 2. The latter are of relevance insofar as the ^{127}I elastically scattered ions equilibrated in Au, while the evaporation residue ions equilibrated in Ni. The efficiencies were corrected for these differences in mean charge state by comparison of results of measurements of elastic scattering and evaporation residue charge distributions. These yield distributions were obtained by varying the charge-state values used in the field setting equations over ranges of values spanning those given by Eq. (1).

Representative q-dependent yield profiles are displayed in Fig. 4. As expected, the peak elastic scattering yield is shifted by about one charge state towards higher q from the value given by Eq. (1), reflecting the influence of the above-mentioned chromatic aberrations. The aspect of importance in Fig. 4 is the shift of the peak evaporation residue yield by approximately one charge-state relative to the peak elastic scattering yield; this peak yield shift is consistent with measured[19] mean charge states for ^{127}I in Ni and Au at $v_r \sim 0.57$. The correction to the efficiencies is given by the ratio of elastic-to-fusion yields at the mean charge state $\bar{q}$ [Eq. (1)]; the corresponding uncertainty is given by the variations in this ratio due to uncertainties in the charge-state shift $\Delta i = i_{q(\text{peak-el})} - i_{q(\text{peak-fus})}$. We find that there is a 7% uncertainty in the corrected efficiencies due to possible variations in the charge-state shift Δi of a factor of 2.

This 7% error and the 3.6% calibration error could be reduced in future measurements by constructing and using a more reliable mean-charge state algorithm and by removing the fore magnetic quadrupole doublet. The former would minimize discrepancies due to the inadequate energy and

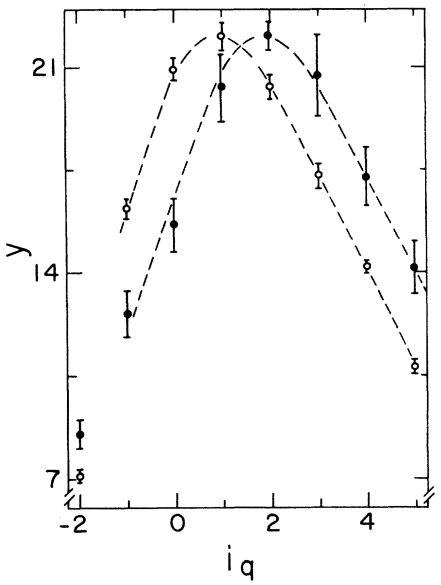

FIG. 4. Relative yields for different charge-state settings. Note the suppressed origin of the ordinate axis. The zero of the abscissa represents the mean charge state given by Eq. (1), and i_q the shift in charge-state units. Open circles denote ^{127}I + Au elastic scattering yields; filled circles denote ^{58}Ni + ^{58}Ni evaporation residue yields normalized to the same peak value as the elastic scattering yields. Dashed lines denote the smoothed yield distributions used for efficiency correction and error estimate purposes.

target dependence of Eq. (1). The latter would reduce the associated variations in yield but, due to the resulting loss in focusing, would lead to an increase in the number of background events as well.

B. Complete fusion

The measurements of the evaporation residue differential cross sections are summarized in Table II. Zero degree differential cross sections, summed over the recoil spectra, are listed in column 2. Representative recoil kinetic energy spectra are displayed in Fig. 5. The uniformity of these spectra is apparent. We find from summation of these spectra that approximately 45% of the total yield was obtained in a given run with the velocity selector set for energies near that of the center of mass. The recoil kinetic energies were obtained from the velocities assuming that the evaporation residue products have mass number $A = 113$, and are approximate for other evaporation residues. The uncertainty to the conversion of yield to absolute cross section due to imprecise evaporation residue mass and atomic number identification is negligible (the large negative Q value for Ni-Ni fusion results in low compound nucleus excitation energies which, in turn, leads to a narrow spectrum of evaporation residue product nuclides).

Angular distributions of the evaporation residues

TABLE II. Summary of zero degree differential cross sections and measurements performed.

E_{lab} (MeV)	ER $\frac{d\sigma}{d\Omega}(\theta = 0°)$ (b/sr)	Spectra	Angular distribution
187.6	0.0125 ± 0.0049		
188.0	0.0245 ± 0.0072		
189.0	0.0888 ± 0.0222		
190.0	0.226 ± 0.0255		
191.0	0.469 ± 0.0502		
192.0	0.634 ± 0.0423		
193.0	1.25 ± 0.135		
194.0	1.60 ± 0.045	X	X
	1.63 ± 0.062		
196.0	2.74 ± 0.159		
198.0	4.75 ± 0.225		
200.0	6.80 ± 0.290		
	6.88 ± 0.480		
202.0	8.96 ± 0.288	X	X
205.0	16.24 ± 0.941		
207.0	17.93 ± 0.956		
210.0	25.50 ± 0.685	X	X
215.0	32.97 ± 1.15		
220.0	45.33 ± 2.35	X	X

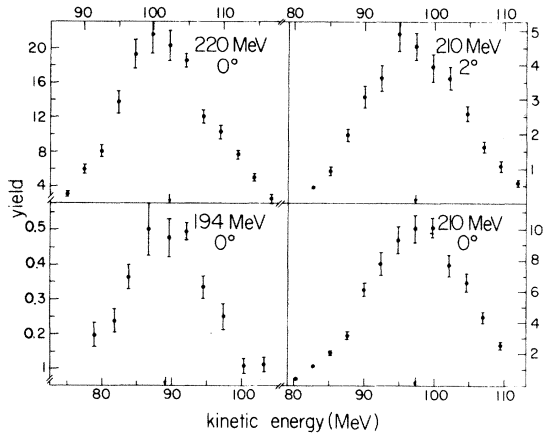

FIG. 5. Recoil kinetic energy spectra of the evaporation residues at representative bombarding energies and recoil angles. Arrows denote the energies of the center of mass corrected for energy loss in the targets.

are presented in Fig. 6. We find from integration of these angular distributions that more than 90% of the total yield is forward of 3°. As a consequence of the sharp dropoff occurring with increasing recoil angle and the 1 msr solid angle we employed lab angles weighted by the angular distribution in constructing the angular distributions.

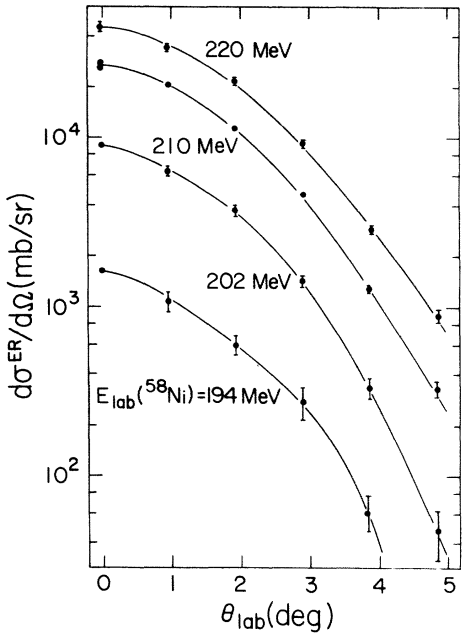

FIG. 6. Angular distributions of the evaporation residues at various bombarding energies. Solid lines denote the smoothed angular distributions used for integration purposes.

We converted the supplemental zero degree differential cross sections to complete fusion cross sections using the smoothed results of the angular distribution integration. The complete fusion cross sections are listed in Table III and are displayed in Fig. 7. The average center-of-mass energies were weighted by the excitation function and were corrected for energy loss in the targets using the Northcliffe-Schilling tables.[20]

In most instances the statistical errors are smaller than or comparable to the circles shown in Fig. 7. For these data the principal contributions to the total errors are the 3.6% uncertainty to the absolute efficiencies and the 7% uncertainty associated with the mean charge-state identification. The uncertainty in the spectral summations is 1.7% and the uncertainty in the angular distribution integrations is 2.1%. Combining these errors in quadrature gives total errors ranging from 8% for the most extensive data to 10% for the least extensive data. For those data with larger statistical uncertainties larger errors were assigned accordingly. It should be noted that the evaporation residue events were identified in terms of their energy loss and total energy in the telescope after velocity filtering, and are consequently free from background events due to either other $^{58}Ni + {}^{58}Ni$ reactions or carbon/oxygen contaminant reactions.

The critical angular momenta for fusion, $l_{cr}(E_{c.m.})$, is defined within the framework of the sharp-cutoff approximation as[21]

$$\sigma^{CF} = \pi\lambda^2(l_{cr}+1)^2 . \tag{4}$$

TABLE III. Summary of evaporation residue cross sections.

E_{lab} (MeV)	$\bar{E}_{c.m.}$ (MeV)	σ^{ER} (mb)	$\Delta\sigma^{ER}$ (%)	l_{cr} ($\hbar$)
187.6	93.25	0.049	40	
188.0	93.45	0.096	30	
189.0	93.88	0.348	25	
190.0	94.31	0.888	15	
191.0	94.76	1.86	15	
192.0	95.22	2.52	10	
193.0	95.68	4.98	15	
194.0	96.15	6.47	8	
196.0	97.10	11.1	10	
198.0	98.05	19.5	10	
200.0	99.02	28.6	10	
202.0	100.0	37.3	8	
205.0	101.5	71.2	10	17 ± 1
207.0	102.5	79.9	10	18 ± 1
210.0	103.9	120	8	22 ± 1
215.0	106.4	159	10	26 ± 1
220.0	108.9	226	8	32 ± 1

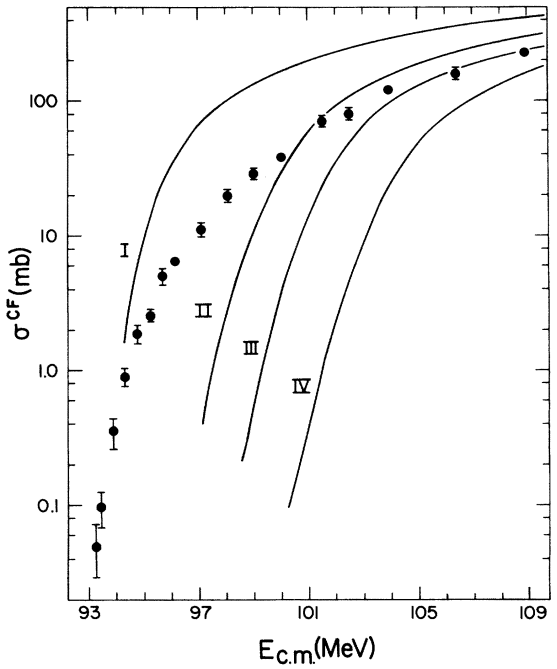

FIG. 7. The excitation function for complete fusion of $^{58}Ni + {}^{58}Ni$ as a function of the weighted average center-of-mass energy. Error bars represent total errors. Smooth curves denote surface-surface interaction calculations using the I: S-WW (Ref. 26) potential; II: Bass (Ref. 25) potential; III: KNS (Ref. 24) potential; and IV: proximity potential (Ref. 23).

Values for l_{cr} obtained from the experimental cross sections σ^{CF} using Eq. (4) are listed in column 5 of Table III. The concept of an l_{cr} is not particularly useful at center-of-mass energies near and below that of the fusion barrier: For massive target-projectile combinations the centrifugal barrier rises slowly with increasing angular momenta at low angular momenta and the corresponding transmission coefficients decrease slowly. Therefore, l_{cr} values have been given in Table III for data at above-barrier energies only.

We wish to determine to what extent the cross sections for complete fusion of ^{58}Ni with ^{58}Ni at sub-barrier energies can be described by simple barrier penetration by spherical, liquid-drop nuclei. To accomplish this we compared our experimental results to those calculated in an adiabatic, barrier penetration model. In this model (i) the attractive nuclear potential was taken to be that of a surface-surface interaction, and (ii) the contribution of each partial wave to σ^{CF} was determined solely by the transmission coefficients $T_l(E_{c.m.})$, i.e.,

$$\sigma^{CF} = \pi\lambda^2 \sum_l (2l+1)T_l , \tag{5}$$

where λ is the reduced de Broglie wavelength of

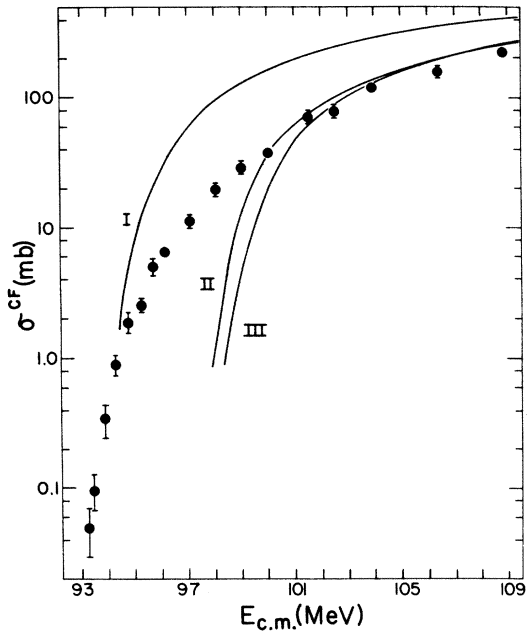

FIG. 8. The excitation function for complete fusion of ^{58}Ni + ^{58}Ni. Data as in Fig. 7. Smooth curves denote S-WW (Ref. 26) calculations using I: $R_0 = 1.137$ fm, $b_{surf} = 17$ MeV; II: $R_0 = 1.018$ fm, $b_{surf} = 19$ MeV; III: $R_0 = 1.074$ fm, $b_{surf} = 17$ MeV. (The matter radius constant R_0 is related to R_a by $R_a = R_0 A_a^{1/3}$. In Ref. 26 the expression $R_a = 1.28A_a^{1/3} - 0.76 + 0.8A_a^{-1/3}$ was used, which for ^{58}Ni is equivalent to $R_0 = 1.137$ fm.) The effective fusion barrier deduced from the normalized S-WW model calculations was 99.0 ± 0.6 MeV. The precise value for the barrier depends upon the model and potential used in the analysis. The barrier, averaged over values extracted using several formulations, was 99.5 ± 1.5 MeV. For comparison, the barriers corresponding to the un-normalized model calculations presented in Fig. 7 are 95.3, 99.2, 100.9, and 103.5 MeV, for excitation functions labeled I to IV, respectively.

the incident ion. By approximating the shape of the interaction barrier by that of an inverted harmonic oscillator we were able to employ Hill-Wheeler[22] transmission coefficients

$$T_l(E_{c.m.}) = \left\{1 + \exp\left[\frac{2\pi}{\hbar\omega_l}(V_l - E_{c.m.})\right]\right\}^{-1}, \tag{6}$$

where $V_l(R_l)$ is the barrier height for the lth partial wave. The quantity R_l is its radial position and $\hbar\omega_l$ is its curvature,

$$\hbar\omega_l = \left|\frac{\hbar^2}{\mu}\frac{d^2V_l}{dR_l^2}\right|_{R_l = R_l(V_l^{max})}^{1/2}, \tag{7}$$

evaluated at the barrier maximum V_l^{max}. The interaction potential is the sum of nuclear, Coulomb, and centrifugal potentials:

$$V(l, r) = V_N(r) + \frac{Z_T Z_P e^2}{r} + \frac{\hbar^2 l(l+1)}{2\mu r^2}. \tag{8}$$

There are several widely used surface-surface potentials. One such potential is the proximity potential of Błocki *et al.*[23] Another is the generalized liquid-drop potential of Krappe, Nix, and Sierk (KNS).[24] Two other surface-surface potentials are the Bass[25] potential and the Siwek-Wylczynska and Wylczynski[26] (S-WW) potential. The quantities V_l, R_l, and $\hbar\omega_l$ were fit to these four interaction potentials for each partial wave, and the cross sections for complete fusion were then calculated using Eqs. (5) and (6).

At above-barrier energies where σ^{CF} appears to behave classically, i.e., above energies of about 101 MeV, the best agreement with the data was obtained (see Fig. 7) using the KNS[24] potential (which is free of adjustable parameters). Good agreement with above-barrier fusion data has been obtained[27,28] using the proximity potential with minor adjustments of the matter radius. The S-WW potential was adjusted in this manner to enable us to compare data to calculations which similarly reproduced the observed high energy behavior. Representative results[29] are presented in Fig. 8. As can be seen from Figs. 7 and 8, comparable amounts of barrier penetration are predicted by the various surface-surface interaction potentials, when placed on a common scale with respect to the data. The main point to be drawn from these figures is that substantially more sub-barrier fusion is being observed experimentally than can be accounted for in terms of adiabatic barrier penetration involving spherical, liquid-drop nuclei.

The extent of the sub-barrier fusion is significant as ^{58}Ni + ^{58}Ni is a nearly closed-shell, symmetric target-projectile system and one might expect minimal barrier penetration. In Ref. 30 the widespread occurrence in systems with $A_P \leq 40$ of sub-barrier fusion beyond that given by liquid-drop barrier penetration estimates was noted. More specifically,[30,31] slight departures of the excitation functions calculated in a barrier penetration model from those observed experimentally occurred in systems involving light projectiles and targets, while considerably larger departures occurred in systems having larger $Z_P Z_T$. The extensive sub-barrier fusion observed in the present work with the massive ^{58}Ni projectiles may be partly a consequence of dynamic polarization. It may well be that the fusion dynamics and underlying multidimensional potential energy surface preclude any useful description in terms of adiabatic, one-dimensional barrier penetration. TDHF calculations may provide valuable insight into the mechanism by which massive nuclei fuse at sub-barrier energies; such calculations will be presented together with data on Ni and Ge sub-

barrier fusion in a forthcoming publication.

In Ref. 11 we demonstrated that the valence neutrons have a major influence upon the fusion process at near- and sub-barrier energies. In other recent works[9,10] the possible influence of ground-state deformations upon the excitation functions for complete fusion of ^{16}O and ^{40}Ar projectiles with Sm targets was investigated. It is noteworthy that substantial differences between excitation functions involving ^{16}O projectiles and those involving ^{40}Ar projectiles were seen.[10] We may conclude that the cross sections for complete fusion of massive nuclei at sub-barrier energies are sensitive to the underlying nuclear structure, to the dynamics of the fusion process, and to the interplay between these two aspects.

The values for the fusion barrier given in the caption to Fig. 8 are estimates, presented to delineate the sub-barrier regime. At the barrier, the complete fusion cross sections are a few tens of millibarns; the measured cross sections span a range of three orders of magnitude below the barrier values. The effective barrier estimates were made from model fits to above-barrier data. Such analyses do not incorporate those dynamic and structural aspects discussed above which seem to dominate the process of barrier penetration. A detailed investigation of the height, position, and shape of the fusion barrier, as probed by broad-range sub-barrier measurements, is in progress.

IV. SUMMARY

The excitation function for complete fusion of ^{58}Ni with ^{58}Ni has been determined with high precision at near- and sub-barrier energies using the MIT-BNL Velocity Selector in conjunction with a gas telescope. The measured complete fusion cross sections ranged in magnitude from 50 μb at 93.3 MeV to 230 mb at 108.9 MeV. The cross sections for sub-barrier fusion were found to be surprisingly large when compared to those given by simple penetrability considerations. We then pointed out that the cross sections for complete fusion of massive nuclei at sub-barrier energies are sensitive to the underlying nuclear structure, to the dynamics of the fusion process, and to the interplay between these two aspects.

ACKNOWLEDGMENTS

The authors wish to thank Professor A. K. Kerman, Dr. H. J. Krappe, and Professor L. Grodzins for many helpful discussions. The authors also wish to thank Dr. H. J. Krappe for supplying some of the model calculations presented herein. This work was supported by the U. S. Department of Energy under Contract No. ACO2-76ERO3069.

[1] H. H. Gutbrod, W. G. Winn, and M. Blann, Nucl. Phys. A213, 267 (1973).
[2] R. L. Kozub, N. H. Lu, J. M. Miller, D. Logan, T. W. Debiak, and L. Kowalski, Phys. Rev. C 11, 1497 (1975).
[3] Y. Eyal, M. Beckerman, R. Chechik, Z. Fraenkel, and H. Stocker, Phys. Rev. C 13, 1527 (1976).
[4] B. Sikora, J. Bisplinghoff, W. Scobel, M. Beckerman, and M. Blann, Phys. Rev. C 20, 2219 (1979).
[5] J. D. Garrett, H. E. Wegner, T. M. Cormier, E. R. Cosman, and A. J. Lazzarini, Phys. Rev. C 12, 481 (1975).
[6] T. M. Cormier, E. R. Cosman, A. J. Lazzarini, H. E. Wegner, J. D. Garrett, and F. Pühlhofer, Phys. Rev. C 15, 654 (1977).
[7] F. Pühlhofer, W. F. W. Schneider, F. Busch, J. Barrette, P. Braun-Munzinger, C. K. Gelbke, and H. E. Wegner, Phys. Rev. C 16, 1010 (1977).
[8] D. Horn, H. A. Enge, A. Sperduto, and A. Graue, Phys. Rev. C 17, 118 (1978). C. Bolton, W. A. Schier, N. Tsoupas, H. Enge, M. Salomaa, A. Sperduto, and A. Graue, *ibid.* 18, 293 (1978).
[9] R. G. Stokstad, Y. Eisen, S. Kaplanis, D. Pelte, U. Smilanski, and I. Tserruya, Phys. Rev. Lett. 41, 465 (1978); Phys. Rev. C 21, 2427 (1980).
[10] R. G. Stokstad, W. Reisdorf, K. H. Hildenbrand, J. V. Kratz, G. Wirth, R. Lucas, and J. Poitou, Z. Phys. A 295, 269 (1980).
[11] M. Beckerman, M. Salomaa, A. Sperduto, H. Enge, J. Ball, A. DiRienzo, S. Gazes, Yan Chen, J. D. Molitoris, and Mao Nai-feng, Phys. Rev. Lett. 45, 1472 (1980).
[12] M. Salomaa and H. A. Enge, Nucl. Instrum. Methods 145, 279 (1977); H. A. Enge and D. Horn, *ibid.* 145, 271 (1977).
[13] H. A. Enge, Nucl. Instrum. Methods 162, 161 (1979).
[14] V. S. Nikolaev and I. S. Dmitriev, Phys. Lett. 28A, 277 (1968).
[15] H.-D. Betz, Rev. Mod. Phys. 44, 465 (1972).
[16] S. B. Kowalski, unpublished.
[17] L. Grodzins, R. Kalish, D. Murnick, R. J. Van de Graaff, F. Chmara, and P. H. Rose, Phys. Lett. 24B, 282 (1967).
[18] S. Datz, C. D. Moak, H. O. Lutz, L. C. Northcliffe, and L. B. Bridwell, At. Data 2, 273 (1971).
[19] A. DiRienzo, M.S. thesis, MIT, 1980 (unpublished).
[20] L. C. Northcliffe and R. F. Schilling, Nucl. Data A7, 223 (1970).
[21] For identical target-projectile combinations one should use $(l_{cr}+1)(l_{cr}+2)$ in place of $(l_{cr}+1)^2$; however, for the number of partial waves involved, there is little difference in the l_{cr} values deduced using these two ex-

pressions.
[22]D. L. Hill and J. A. Wheeler, Phys. Rev. 89, 1102 (1953).
[23]J. Błocki, J. Randrup, W. J. Swiatecki, and C. F. Tsang, Ann. Phys. (N.Y.) 105, 427 (1977).
[24]H. J. Krappe, J. R. Nix, and A. J. Sierk, Phys. Rev. Lett. 42, 215 (1979); Phys. Rev. C 20, 992 (1979).
[25]R. Bass, Phys. Rev. Lett. 39, 265 (1977).
[26]K. Siwek-Wylczynska and J. Wylczynski, Phys. Lett. 74B, 313 (1978); J. Wylczynski and K. Siwek-Wylczynska, *ibid.* 55B, 270 (1975).
[27]J. R. Birkelund, J. R. Huizenga, J. N. De, and D. Sperber, Phys. Rev. Lett. 40, 1123 (1978).
[28]L. C. Vaz and J. M. Alexander, Phys. Rev. C 18, 2152 (1978).
[29]The S-WW potential presented in Ref. 26 is of the Woods-Saxon form $V_N(r)=-Vf_{WS}(r, C_T+C_p, a)$ with $V=b_{surf}[A_T^{2/3}+A_p^{2/3}-(A_T+A_p)^{2/3}]$ and $a=V/16\pi\gamma\bar{C}$, where γ is a surface tension constant and $\bar{C}$ is the reduced radius of curvature. The quantities C_T and C_p are central radii, related to equivalent sharp radii R_a by $C_a=R_a(1-1/R_a^2)$. Numerical constants are given in the caption to Fig. 8 [cf., Ref. 23 and W. D. Myers and W. J. Swiatecki, Ark. Fys. 36, 343 (1967); W. D. Myers, Nucl. Phys. A204, 465 (1973)].
[30]L. C. Vaz, J. M. Alexander, and G. R. Satchler (unpublished).
[31]H. J. Krappe, Lecture Notes in Physics 117, 312 (1980).